

Article

Optimization of Installation Position for Complex Space Curve Weldments in Robotic Friction Stir Welding Based on Dynamic Dual Particle Swarm Optimization

Guanchen Zong , Cunfeng Kang * , Shujun Chen and Xiaoqing Jiang 

College of Mechanical and Energy Engineering, Beijing University of Technology, Beijing 100124, China; zongguanchen@emails.bjut.edu.cn (G.Z.); sjchen@bjut.edu.cn (S.C.); xjiang@bjut.edu.cn (X.J.)

* Correspondence: kangcunfeng@bjut.edu.cn

Abstract: Robotic friction stir welding (RFSW), with its wide application range, ample working space, and task flexibility, has emerged as a vital development in friction stir welding (FSW) technology. However, the low stiffness of serial industrial robots can lead to end-effector deviations and vibrations during FSW tasks, adversely affecting the weld quality. This paper proposes a dynamic dual particle swarm optimization (DDPSO) algorithm through a new comprehensive stability index that considers both the stiffness and vibration stability of the robot to optimize the installation position of complex space curve weldments, thereby enhancing the robot's stability during the FSW process. The algorithm employs two independent particle swarms for exploration and exploitation tasks and dynamically adjusts task allocation and particle numbers based on current results to fully utilize computational resources and enhance search efficiency. Compared to the standard particle swarm optimization (PSO) algorithm, the DDPSO approach demonstrated superior search capabilities and stability of optimization results. The maximum fitness value improved by 4.2%, the average value increased by 12.74%, and the concentration level of optimization results rose by 72.91% on average. The new optimization method pioneers fresh perspectives for optimizing the stability of RFSW, providing significant grounds for the process optimization and offline programming of complex spatial curve weldments.



Citation: Zong, G.; Kang, C.; Chen, S.; Jiang, X. Optimization of Installation Position for Complex Space Curve Weldments in Robotic Friction Stir Welding Based on Dynamic Dual Particle Swarm Optimization.

Processes **2024**, *12*, 536. <https://doi.org/10.3390/pr12030536>

Academic Editors: Qian Zhi and Rogante Massimo

Received: 9 February 2024

Revised: 29 February 2024

Accepted: 6 March 2024

Published: 7 March 2024



Copyright: © 2024 by the authors. Licensee MDPI, Basel, Switzerland. This article is an open access article distributed under the terms and conditions of the Creative Commons Attribution (CC BY) license (<https://creativecommons.org/licenses/by/4.0/>).

Keywords: friction stir welding; robot stability index; robot stiffness; vibration stability; Cartesian stiffness ellipsoid

1. Introduction

Friction stir welding (FSW) technology, as an advanced solid-phase welding technique, has been widely used in aerospace, automotive manufacturing, and shipbuilding owing to its advantages, such as broad material applicability, minimal residual stress, and lower welding temperature [1,2]. Traditional FSW equipment is generally developed using CNC machines [3]. While it offers high accuracy and strong structural stiffness, its limited workspace restricts the welding of complex workpieces [4]. Industrial robots, with their strong versatility, large working space, and low development costs, have already been widely applied in the welding field [5]. The integration of general industrial robots with FSW equipment has become an inevitable trend in the development of FSW [6]. However, due to the high welding force in FSW and the limited end stiffness of serial industrial robots, stability during FSW decreases, leading to welding errors from excessive end displacement and reduced welding quality due to vibration [7–9]. These factors have become the main obstacles hindering the further development and widespread application of RFSW technology.

There are valuable studies to solve the problem of end displacement in FSW robots. To reduce the impact of robot end displacement, offline programming methods were used to pre-compensate for end errors in the RFSW process. Kolegain et al. [10] proposed a

deflection model-based feedforward compensation technique and an offline path planning using Bézier curves to solve the position and orientation deviations of the robot end effector during welding. Bai et al. [3] presented a method for predicting and compensating for the end displacement of FSW robots to solve the problem of insufficient plunge depth. Other scholars are committed to reducing the welding errors of RFSW through online compensation methods. Li et al. [11] developed a laser circular scanning-based multiparameter sensing technique for five-axis RFSW. This method effectively tackles the limitations of existing sensing techniques to accurately measure plunge depth and seam deviation. Soron et al. [12] established an RFSW system using a force control algorithm on the ABB IRB-7600-500 robot platform and achieved the anticipated welding accuracy.

Some scholars have studied the impact of vibration on the friction stir welding process. Rahmi et al. [13] proposed an improved FSW process, named friction stir vibration welding (FSVW). By applying vibration to the workpiece during the FSW process, experimental results showed that FSVW could significantly improve the microstructure and mechanical properties of the weld. Bagheri et al. [14] investigated the mechanical behavior and microstructure of AA6061-T6 joints manufactured by the FSVW technique. The results indicated that, compared to FSW, the FSVW technique could significantly enhance the strength and hardness of the joints. Abbasi et al. [15] explored the effects of vibration on dynamic recrystallization during the magnesium alloy FSVW process through numerical simulation and experimental methods. The results suggested that compared to traditional FSW, vibration could promote nucleation and grain growth, improve grain refinement, and thus affect the microstructure and mechanical properties of the weld zone.

Current research regarding vibrations caused by insufficient robot stiffness during welding is relatively scarce. Yu [16] analyzed the vibration signals of the RFSW process and pointed out that the feeding direction affected the vibration, but further research has not been conducted. Like RFSW, robotic milling also uses general industrial robots as the working platform. More research has been conducted on the vibration phenomenon during robotic milling processes. These studies mainly focused on vibration detection and signal analysis [17], pose optimization [18], active vibration suppression [19], and robot structure optimization [20]. Due to milling characteristics, the vibration was mainly manifested by chatter and regenerative chatter during the machining process [21]. However, periodic forces acting on the stirring tool were still observed during the FSW process. It was suggested that the reason for the periodic forces is the eccentricity error of the stirring pin relative to the electric spindle [22]. Eccentricity errors arise from the stirring tool's positional deviation during installation and wear-induced clearance within the electric spindle under high-load operation. This is an inherent characteristic of FSW and cannot be eliminated [23]. Some researchers have found that a moderate eccentricity error can promote material flow and improve welding quality [24]. However, excessive eccentricity errors can worsen welding quality, increase welding defects, and increase welding force fluctuations [25]. Traditional FSW equipment utilizing CNC machines typically features high stiffness, making the mechanical structure largely unaffected by fluctuations in welding force [26]. However, in RFSW systems employing serial industrial robots, excessive welding force fluctuations may lead to end vibrations, undermining welding stability and quality [8].

Current research on stability optimization in RFSW mainly focuses on enhancing robot stiffness, which varies with the robot's pose. Studies have concentrated on optimizing the RFSW welding trajectory to maintain the robot in a position of optimal stiffness throughout the welding process. Jain et al. [27] studied the lateral displacement of the robot's end during the welding process. A method was proposed to determine an optimal workspace of operation by minimizing the lateral deflection errors in the position and orientation of the end effector during FSW. This method can calculate the weld seam's starting position or optimal welding direction to achieve the best welding quality. Zhao et al. [28] studied robot stiffness in various poses and created an ellipsoidal end stiffness model. They introduced a method leveraging the sigmoid function to adjust stiffness based on dexterity or joint

limits, optimizing robot poses for welding tasks to improve end stiffness and flexibility. Xiao et al. [29] studied the strategies to enhance the axial stiffness of a hybrid FSW robot, and a workpiece position optimization method based on the optimal stiffness interval was proposed to maintain a relatively optimal axial stiffness posture of the robot during the welding process.

Current research on RFSW optimization mainly addresses the robot's end effector deviations, neglecting vibration's impact on stability. The research often focuses on simple welds, overlooking complex space curve weldments with more practical relevance. This study addresses the stability issues of serial industrial robots in the FSW process due to low stiffness, introducing a dynamic dual particle swarm optimization algorithm. By optimizing the installation position of complex space curve weldments through a novel stability index, it enhances the robot's stability in the FSW process. The rest of this study is organized as follows. Section 2 describes the environment and steps of the RFSW welding stability experiment and analyzes the results. In Section 3, based on experimental conclusions and the stiffness characteristics of the robot, the method for establishing a comprehensive stability index is explained and validated. In Section 4, the comprehensive stability function of the weldment is used as the fitness function. Optimization was conducted using both the standard PSO algorithm and the DDPSO algorithm. The comparison of the results confirmed DDPSO's effectiveness, and the weldment's optimal position was obtained. Section 5 summarizes the research.

2. RFSW Stability Experiment and Analysis

Due to the serial characteristics, industrial robots exhibit significant variations in Cartesian stiffness at the robot end effector in different directions [28]. The following experiments were designed to study the effect of different feed directions on the welding quality of RFSW.

Figure 1 shows the experimental platform used in this study. Figure 1c is a heavy-duty FSW robot equipped with a dedicated electric spindle at the robot's end. The stirring tool used in the experiment is shown in Figure 1f, with a conical stirring pin of 5 mm. Figure 1e shows that the accelerometer was fixed in the x, y, and z directions near the stirring tool at the end of the electric spindle. The accelerometers were connected to the computer through an amplifier and a data acquisition card to record vibration signals during welding. The sampling rate of the vibration signal was 25,000 Hz. The relative position between the workpiece and the robot is shown in Figure 1c. The workbench (Figure 1a) was located 2.1 m in the negative y direction of the robot, and the workbench height was 0.7 m in the positive z direction. An AA6061-T6 aluminum alloy plate with $300 \times 150 \times 5$ mm dimensions was welded. The welding direction is shown in Figure 1b, and the welding was carried out along +x, -x, +y, and -y on the same plate.

To make the fluctuation of welding force more obvious while avoiding the natural frequency of the robot to prevent resonance, the welding parameters of this study were a spindle speed of 2200 rpm, a feed rate of 2 mm/s, and a tilt angle of 2° for welding experiments. The eccentricity error of the current stirring tool was 0.05 mm. The welding results are shown in Figure 2a,b. The green dashed line in the figure represents the teaching trajectory of the weld seam, and the red dashed line represents the actual centerline of the weld seam. Observing the trajectory of the weld seam, it was found that the surface of the weld seam in all four feed directions was relatively flat and uniform, but there were varying degrees of deviation. The minimum displacement was about 2 mm along the -x direction, and the maximum was about 7 mm along the +x direction. The error along the +y and -y directions was similar, at about 5 mm. Analyzing the vibration signals during the welding process, it was found that the vibration situation along the four directions was identical under the current parameters.

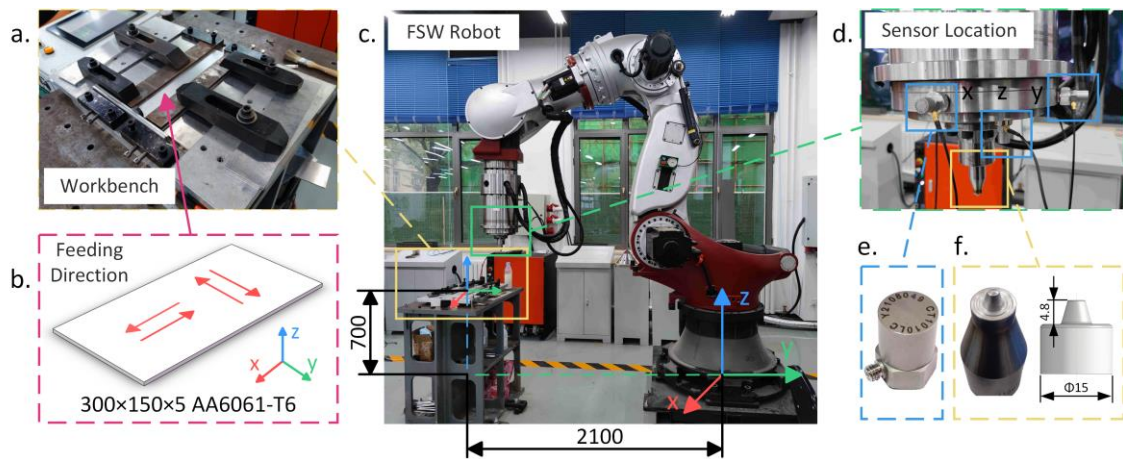


Figure 1. The experiment equipment and relative position of the weldment and the robot. (a) Welding fixture. (b) Weldment dimensions and materials. (c) FSW robot and welding position. (d) Accelerometer mounting position. (e) Accelerometer. (f) Stirring tool.

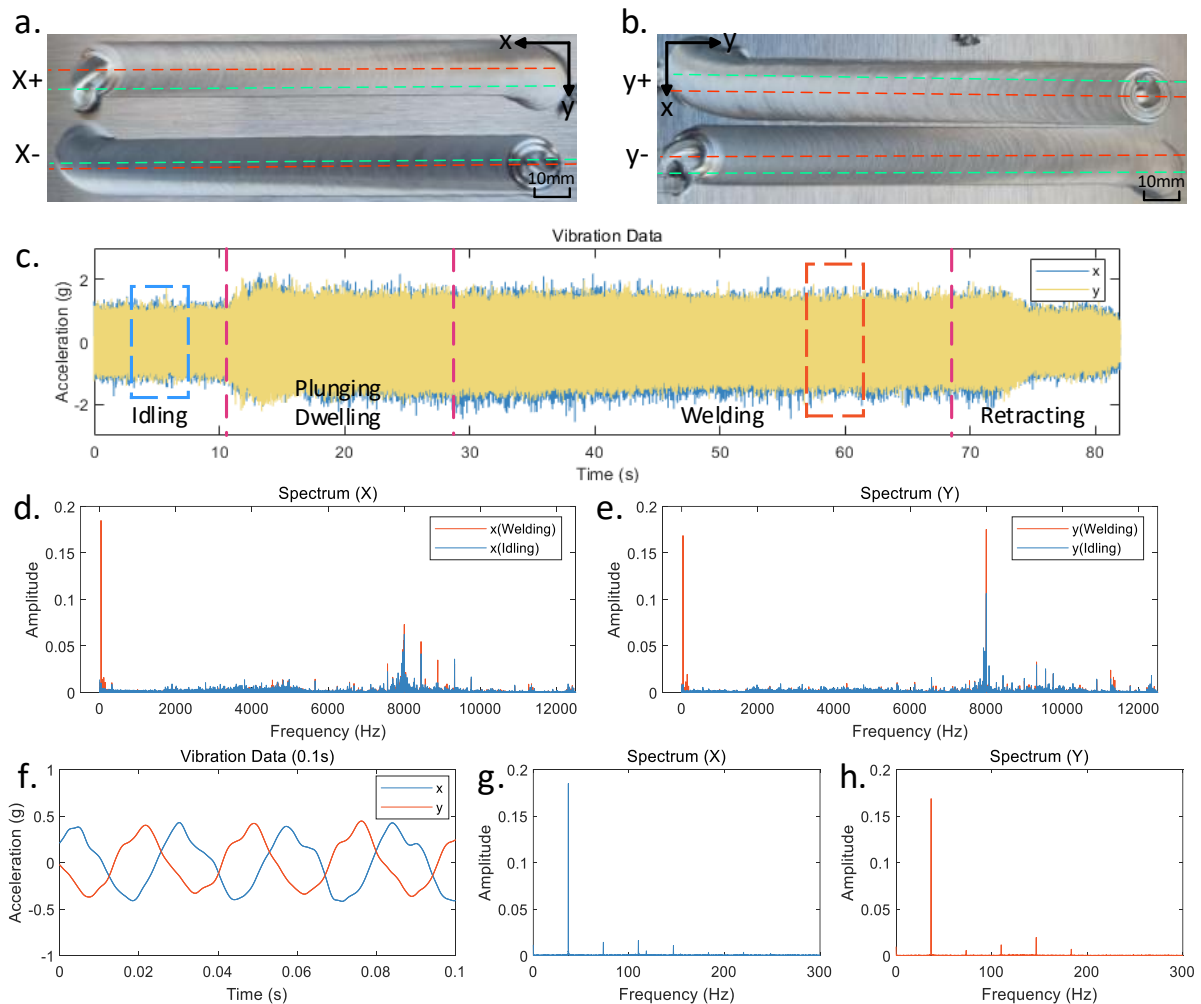


Figure 2. Analysis of the vibration signal. (a) Weld seams along the +x and −x directions. (b) Weld seams along the +y and −y directions. (c) Vibration data of the welding process along the −x direction. (d,e) Comparison of vibration data spectra between idle and welding stages. (f) Vibration data after low-pass filtering. (g,h) Spectrum of low-frequency vibration data.

Due to the periodic fluctuation of welding force during FSW, which was mainly caused by the eccentricity error of the stirring tool [22], the eccentricity error primarily affected the radial movement of the rotating axis. Therefore, this study mainly analyzed the vibration data in the x and y directions. The vibration data of the welding process feed along the $-x$ direction is shown in Figure 2c, with time (s) as the horizontal axis and acceleration (g) as the vertical axis. The welding process was divided into the idle stage, plunging and dwelling stage, welding stage, and retracting stage. The peak value of the vibration signal during the idle stage was around 1.2 g, and the peak value during the welding stage was about 1.8 g. The root mean square (RMS) of the signal was used as the indicator for judging vibration intensity. Taking a signal of about 5 s in length from the middle part of the idle stage as the blue dashed square in Figure 2c, the RMS values in the x direction and y direction during the idle stage were calculated to be 0.353 and 0.360, respectively. Taking the vibration stable signal during the last third of the welding stage for about 5 s as the red dashed square in Figure 2c, with an RMS value of 0.488 in the x direction and 0.507 in the y direction, it can be concluded that the increase in vibration intensity was 38.2% and 40.8%, respectively.

The frequency spectra of vibration signals in the x and y directions during the idle and welding stages were obtained by Fourier transform of the intercepted vibration signals, as shown in Figure 2d,e. The vibration generated by the operation of the electric spindle itself was mainly concentrated in the high-frequency range of 8000 Hz to 10,000 Hz. In contrast, the frequency component added during welding was focused on the low-frequency range. The spectral range of the vibration signals during the welding process was adjusted to 0–300 Hz, as illustrated in Figure 2g,h, indicating that the vibrations during welding were mainly concentrated in the region below 200 Hz. The vibration signal consisted of a fundamental frequency signal with the same frequency as the spindle rotation frequency (36.7 Hz) and harmonic signals with integer multiples of the fundamental frequency. The fundamental frequency component was much greater than the harmonic components. Low-pass filtering on the welding process was performed on the vibration signal with a cutoff frequency of 200 Hz, and the vibration curve is shown in Figure 2f. It can be seen that the vibration signals were relatively smooth, and the vibration period was consistent with the spindle rotation period. It can be concluded that when the eccentricity error of the stirring tool is small, the proportion of vibration generated during the welding process is relatively small, and the impact on welding stability is insignificant. The insufficient stability of the FSW robot is mainly reflected in the weld trajectory error caused by end displacement.

Subsequently, the handle of the stirring tool was grinded to increase the eccentricity error between the stirring pin and the electric spindle to simulate situations such as significant assembly errors or wear of the electric spindle. The eccentricity error between the stirring tool and the electric spindle after grinding was 0.18 mm. Using the same welding parameters, the welding results are shown in Figures 3 and 4. The surface of the weld seam along the $-x$ and $-y$ directions was relatively flat and uniform, but there were different degrees of surface defects in the weld seam along the $+x$ and $+y$ directions. The surface of the weld seam along the $+y$ direction showed changes in appearance characteristics, showing obvious segmentation and changes in the feed direction. The weld seam along the $+x$ direction exhibited a “crawling” phenomenon during welding, which appeared as a fish-scale-like feature on the surface.

The deviations in the weld seam in the four feed directions were similar to those before the increase in the eccentricity error. The vibration signal during the welding process along the $-x$ direction was first analyzed as a comparison. Figure 3b indicates that the vibration signal during the welding process along the $-x$ direction was relatively stable. The peak value of the vibration signal during the welding stage was around 2.5 g. We extracted a vibration signal of about 5 s from the last third of the welding stage as the red dashed square in Figure 3b, with an RMS value of 0.788 in the x direction and 0.767 in the y direction. The vibration intensity increased by 123.2% and 113.1%, respectively, compared

to the idle stage and by 61.5% and 51.3%, respectively, compared to the eccentricity error of 0.05 mm. Fourier transform on the intercepted signal analysis was performed to obtain the vibration signal spectrum, as shown in Figure 3d,e. Compared with an eccentricity error of 0.05 mm, the intensity of the fundamental frequency signal in the vibration signal increased, while the intensity of the harmonic signals significantly increased. The low-pass filtering with a cutoff frequency of 200 Hz was applied to the signal and the vibration curve (Figure 3c). It can be seen that the vibration signal exhibited periodic changes and complex waveforms.

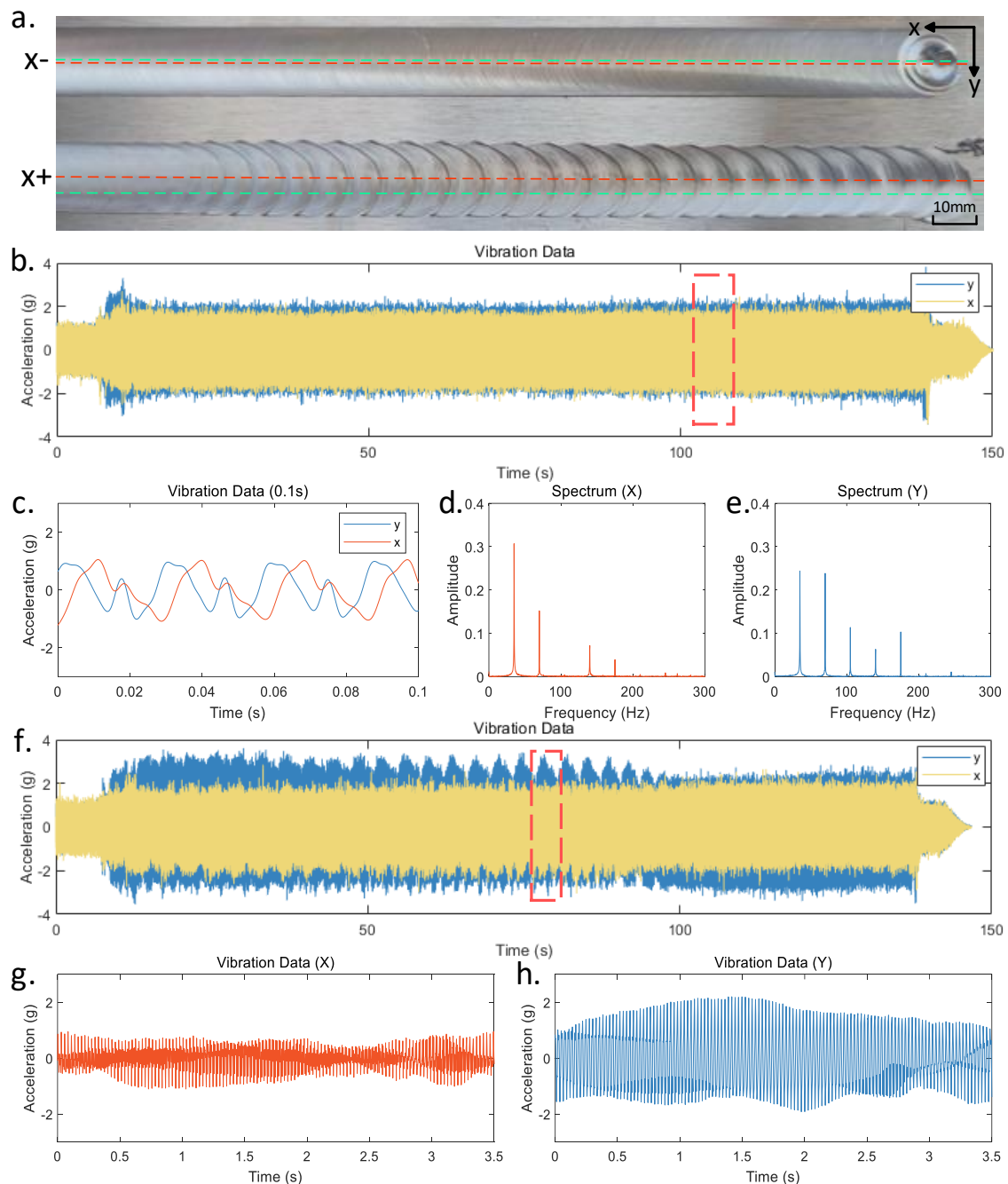


Figure 3. The welding results along the X direction after grinding. (a) Weld seams along the $-x$ and $+x$ directions. (b) Vibration data of the welding process along the $-x$ direction. (c) Vibration data after low-pass filtering along the $-x$ direction. (d,e) Spectrum of low-frequency vibration data. (f) Vibration data of the welding process along the $+x$ direction. (g,h) Vibration data after low-pass filtering along the $+x$ direction.

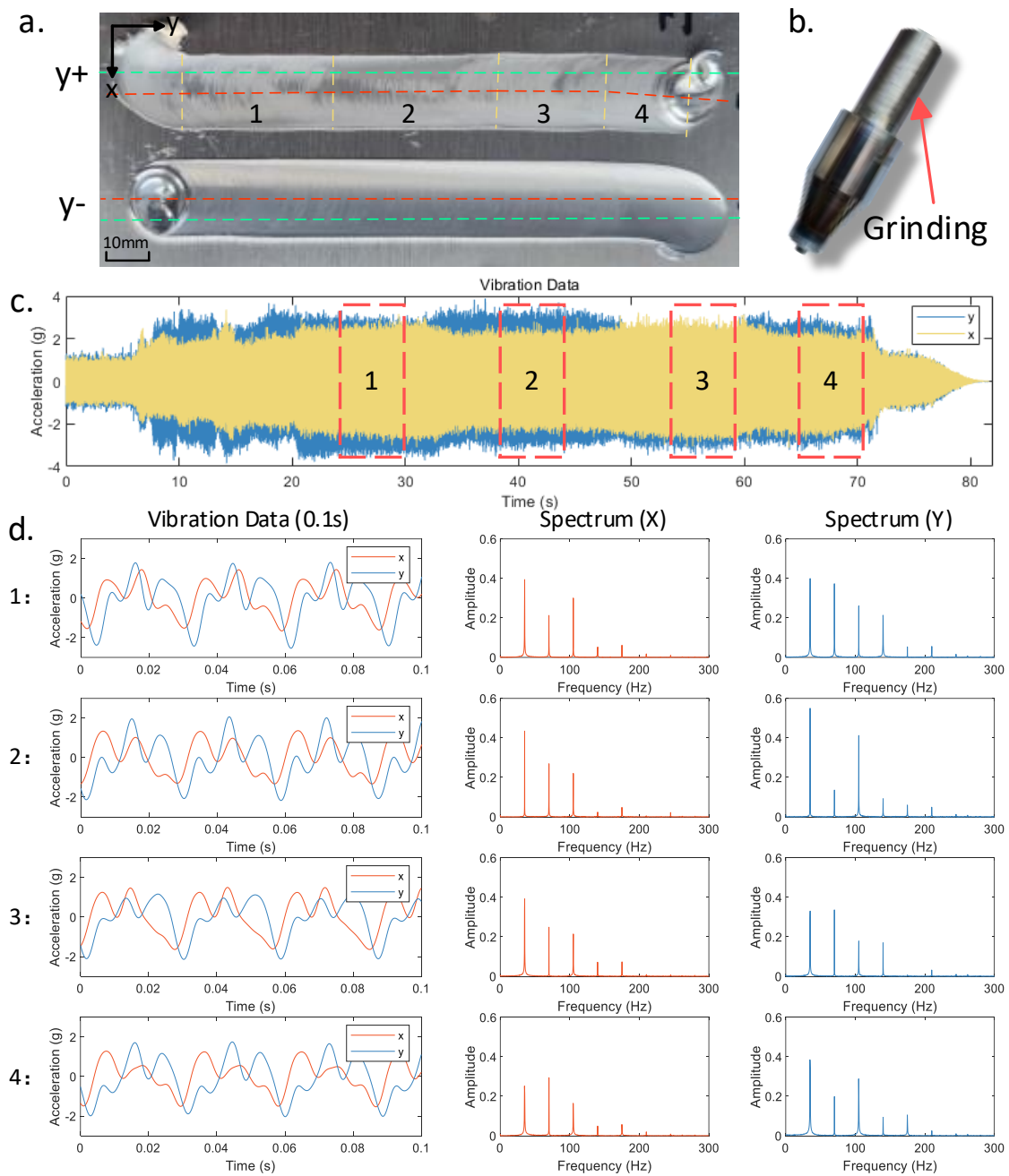


Figure 4. The welding results along the Y direction after grinding. (a) Weld seams along the +y and −y directions. (b) Grinding position of the stirring tool. (c) Vibration data of the welding process along the +y direction. (d) Comparison of vibration data and spectra in four sections along the +y direction.

Next, the vibration signals during the welding process were analyzed along the +y direction (Figure 4c). The vibration signals during the welding stage showed four distinct parts corresponding to Figure 4a. A signal of about 5 s was taken from the middle of each part as the red dashed squares in Figure 4c, and then the Fourier transform was performed to obtain the spectrum. The low-pass filtering served with a cutoff frequency of 200 Hz. Figure 4d shows the vibration curve. The overall vibration signal exhibited periodic changes, but the vibration waveform was more complex, and there were significant differences in the vibration curves between different parts. By comparing the spectrograms, there were substantial differences in the amplitude of the frequency components of different parts

of the vibration signal, with more significant changes in the $-y$ direction. The amplitude of the $-y$ direction frequency component in the first and third parts was relatively similar, and it was relatively similar in the second and fourth parts. It is speculated that during the welding process, as the robot's pose changed, its end switched between two vibration modes, affecting the welded seam's quality. After analyzing the vibration signal in the $+x$ direction during the welding process (Figure 3f), it was found that the vibration signal in the y direction exhibited periodic fluctuations along with the fish-scale-like characteristics during the welding process. The vibration curve is shown in Figure 3g,h after amplifying the signal with one fluctuation period, and low-pass filtering was performed with a cutoff frequency of 200 Hz. It can be observed that the vibration signal period was consistent with the spindle rotation period, but the amplitude showed irregular changes.

The welding process's vibration intensity significantly improved as the stirring tool's eccentricity error increased. Due to the low stiffness and complex structure of robots, the impact of vibration on welding stability became more pronounced. Comparing the welding results in different feed directions, welding along the $-x$ and $-y$ directions can achieve good welding stability. Still, there is a phenomenon of insufficient stability when welding along the $+x$ and $+y$ directions.

Figure 5a shows the force analysis of the FSW process. The force acting on the stirring tool during the welding process can be decomposed into three directions: the axial force F_d along the axis direction, the forward resistance force F_r opposite to the feed direction, and the lateral force F_l generated by the friction between the stirring pin and the base material. The force analyses of the welding process in different feed directions are shown in Figure 5b. Feeding along the $-x$ and $-y$ directions with good welding stability, the force in the y -axis was directed towards the positive direction, which was the direction in which the robot was located. While feeding along the $+x$ and $+y$ directions with poor stability, the force in the y -axis was directed towards the negative direction, which was away from the robot. Therefore, it is speculated that the welding stability of the FSW robot is related to its force direction. The force in the y -axis significantly impacts the welding stability at the current welding position.

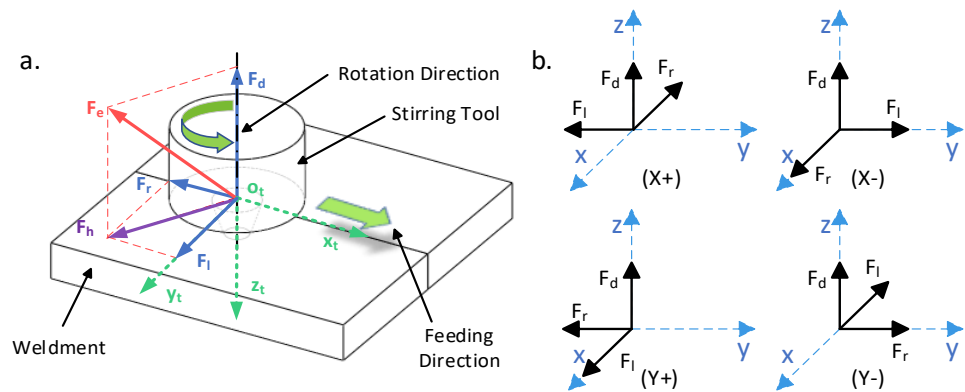


Figure 5. Force analysis during the FSW process. (a) Force analysis of the stirring tool. (b) Force analysis of different feed directions.

3. Comprehensive Stability Index of the FSW Robot

To further analyze the reasons for the influence of feed directions on welding stability and to optimize the feed direction and robot pose, it was necessary to study the directional characteristics of the end effector of the FSW robot. The serial industrial robots exhibited different stiffness characteristics along different directions at the end of the robot due to their structural characteristics. Establishing kinematic and stiffness models of the robot is a prerequisite for studying the end effector's directional stiffness.

3.1. Robot Kinematic and Stiffness Model

The Denavit–Hartenberg (DH) method is the most used approach for establishing a robot kinematic model. Each joint of the FSW robot was moved to its initial position, and a modified DH (MDH) model was established, as illustrated in Figure 6.

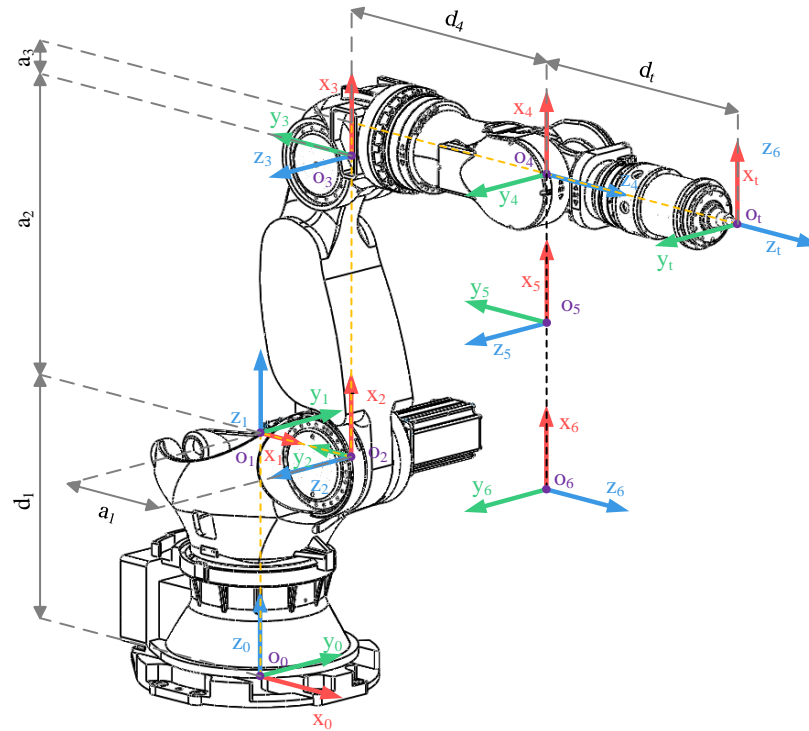


Figure 6. MDH model of FSW robot.

Based on the MDH model and the parameters of the FSW robot, the DH parameters, the joint stiffness, and joint range limits are shown in Table 1.

Table 1. MDH parameters and joint stiffness of the FSW robot.

i	θ_i (°)	d_i (mm)	a_{i-1} (mm)	α_{i-1} (°)	K_θ (N·m/rad)	Joint Limits (°)
1	θ_1	1050	0	0	1.1676×10^6	−180, 180
2	$\theta_2 + 90$	0	500	90	1.2731×10^8	−55, 90
3	θ_3	0	1300	0	1.7187×10^6	−160, 70
4	θ_4	1200	150	90	7.3227×10^5	−360, 360
5	θ_5	0	0	−90	1.1011×10^6	−120, 120
6	θ_6	0	0	90	8.8932×10^5	−360, 360
t	0	1110	0	0	-	-

The homogeneous transformation matrix for adjacent link coordinate systems in the MDH model is defined in Equation (1) [30]:

$${}^i T = R_x(\alpha_{i-1})T_x(a_{i-1})R_z(\theta_i)T_z(d_i) = \begin{bmatrix} c\theta_i & -s\theta_i & 0 & a_{i-1} \\ s\theta_i\alpha_{i-1} & c\theta_i\alpha_{i-1} & -s\alpha_{i-1} & -s\alpha_{i-1}d_i \\ s\theta_i s\alpha_{i-1} & c\theta_i s\alpha_{i-1} & c\alpha_{i-1} & c\alpha_{i-1}d_i \\ 0 & 0 & 0 & 1 \end{bmatrix} \quad (1)$$

where R_x is the coordinate system rotating around the x -axis, T_x is the coordinate system translating along the x -axis, R_z is the coordinate system rotating around the z -axis, T_z is the coordinate system translating along the z -axis, c represents \cos , and s represents \sin .

Homogeneous transformation matrices between links, defined accordingly, can be successively multiplied to yield the transformation matrix from the robot's base coordinate system to its end-effector as Equation (2):

$${}^0_t T = {}^0_1 T(\theta_1) {}^1_2 T(\theta_2) {}^2_3 T(\theta_3) {}^3_4 T(\theta_4) {}^4_5 T(\theta_5) {}^5_6 T(\theta_6) {}^6_t T = \begin{bmatrix} R_t & P_t \\ 0 & 1 \end{bmatrix} \quad (2)$$

where R_t is the rotation matrix of the robot's end effector and P_t is the translation vector of the robot's end effector.

Based on the robot homogeneous transformation matrix, the kinematic model of the robot can be performed. The Jacobian matrix of the robot's end was further derived based on its kinematic model, as given in Equation (3):

$$J = [J_1 \quad J_2 \quad \dots \quad J_6] = \begin{bmatrix} J_{11} & J_{12} & \dots & J_{16} \\ J_{a1} & J_{a2} & \dots & J_{a6} \end{bmatrix} \quad (3)$$

where J_{li} is the Jacobian vector for the movement of the i -th joint and J_{ai} is the rotation Jacobian vector of the i -th joint.

During robotic operation, external forces induced displacements in the end effector, which was attributable to deformations in both joints and links. Given the significantly higher stiffness of the links compared to the joints, link deformations are frequently overlooked in stiffness-related robotic analyses [31].

In robotic joint analyses, the complex composition of motors and reducers is often simplified in the overall stiffness model. Typically, it is represented by a linear torsion spring to approximate the mechanical structure of the joints. Therefore, the joint stiffness model of a six-axis robot can be represented by the diagonal matrix shown in Equation (4) [28].

$$K_\theta = \text{diag}([K_1, K_2, K_3, K_4, K_5, K_6]) \quad (4)$$

From the statics of the robot, the relationship between the joint torque of the robot and the forces at the end effector can be derived from Equation (5):

$$\tau = J^T F \quad (5)$$

where τ is the joint torque of the robot, J^T is the transpose of the Jacobian matrix, and F is the generalized force exerted on the robot end effector.

When subjected to a torque, the deflection of the robot joints is written as Equation (6):

$$dq = K_\theta^{-1} \cdot \tau \quad (6)$$

The formula for calculating the displacement at the robot end effector due to external forces, as a function of joint deflection and end effector displacement, is presented in Equation (7).

$$\Delta X = \begin{bmatrix} \Delta d \\ \Delta \varphi \end{bmatrix} = J \cdot dq = JK_\theta^{-1} J^T F \quad (7)$$

3.2. Robot End Directional Stiffness Index

The influence of the position deviation of the FSW robot's end displacement is much more significant than that of the end effector's pose deviation. Therefore, ignoring the impact of the torque on the end effector's attitude [28], Equation (7) was simplified to Equation (8):

$$\Delta d = J_P K_\theta^{-1} J_P^T f \quad (8)$$

where J_P is the Jacobian matrix of the robot position, representing the first three rows of the Jacobian matrix, $J_P = [J_{11} \quad J_{12} \quad J_{13} \quad J_{14} \quad J_{15} \quad J_{16}]$.

We assumed that the robot's end displacement is in units of displacement, as shown in Equation (9):

$$\|\Delta d\|_2^2 = \Delta d^T \Delta d = f^T C_e^T C_e f = 1 \quad (9)$$

where C_e is the robot end displacement flexibility matrix $C_e = J_P K_\theta^{-1} J_P^T$.

$C_e^T C_e$ is a third-order positive definite real symmetric matrix, which can be obtained by performing eigenvalue decomposition on it, as shown in Equation (10):

$$C_e^T C_e = R_E \begin{bmatrix} \lambda_1 & 0 & 0 \\ 0 & \lambda_2 & 0 \\ 0 & 0 & \lambda_3 \end{bmatrix} R_E^T \quad (10)$$

where R_E is the eigenvector of the matrices and λ_1 , λ_2 , and λ_3 are the eigenvalues of the matrices.

Equation (11) can be obtained by inserting it into Equation (9).

$$f^T R_E \begin{bmatrix} \lambda_1 & 0 & 0 \\ 0 & \lambda_2 & 0 \\ 0 & 0 & \lambda_3 \end{bmatrix} R_E^T f = 1 \quad (11)$$

Equation (11) describes a three-dimensional ellipsoid, as shown in Figure 7a, whose shape will change with the variation in the robot's pose. Supposing $f^T R_E = [x' \ y' \ z']$, Equation (11) can be written in the standard form of an ellipsoidal equation, as given in Equation (12):

$$\frac{x'^2}{a^2} + \frac{y'^2}{b^2} + \frac{z'^2}{c^2} = 1 \quad (12)$$

where $a = \frac{1}{\sqrt{\lambda_1}}$, $b = \frac{1}{\sqrt{\lambda_2}}$, and $c = \frac{1}{\sqrt{\lambda_3}}$.

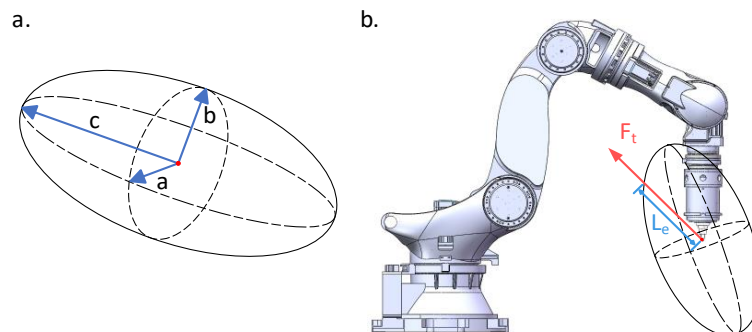


Figure 7. FSW robot end stiffness ellipsoid. (a) The ellipsoid of Equation (12). (b) Stiffness of the robot end effector in the welding force direction.

The half-axis length of an ellipsoid is the reciprocal square root of the eigenvalues of the flexibility matrix, which can reflect the characteristics of the end stiffness of a robot. It is commonly referred to as the Cartesian stiffness ellipsoid of a robot. The shortest half-axis represents the direction of the minimum stiffness at the end of the current robot, and the longest half-axis represents the direction of the maximum stiffness currently. The distance from the center of the ellipsoid to the surface can reflect the stiffness characteristics of the robot end in this direction.

Assuming that during the welding process, the welding force acting on the end of the robot is $F_t = [F_x \ F_y \ F_z]^T$, we converted it to the robot base coordinate system, as represented in Equation (13):

$$F_b = R_t \cdot F_t \quad (13)$$

where R_t is the rotation matrix from the robot base coordinates to the end effector.

Thus, in the current pose of the robot, the distance from the center of the Cartesian stiffness ellipsoid along the welding force direction to the surface of the ellipsoid can be expressed as Equation (14):

$$L_e = \frac{1}{\sqrt{\hat{F}_b^T C_e^T C_e \hat{F}_b}} \quad (14)$$

where \hat{F}_b is the unit vector of F_b , $\hat{F}_b = \frac{F_b}{\|F_b\|}$.

L_e can be used as an evaluation index for the stiffness of the robot's end in the current pose and welding direction, as shown in Figure 7b.

3.3. Robot Vibration Stability Index

The index of robot end stiffness can determine the ability of the robot end to resist deformation in the current pose and force direction. It is generally believed that the larger the value of the robot end to resist deformation, the smaller the deformation at the end of the robot, which is more conducive to improving the machining accuracy of the robot. Therefore, it is often used as an index for robot pose optimization. However, according to the welding experiment along the +y and -y directions shown in Figure 4a, the two opposite-direction welds have similar lateral displacements, indicating that their directional stiffness is not significantly different. At the same time, their vibration stability is quite different. RFSW can reduce the impact of end displacement through offline programming pre-compensation, real-time online compensation, and other methods. The decrease in welding stability caused by vibration is difficult to intervene in through compensation. Therefore, it is necessary to optimize the vibration stability of FSW robots.

Research on robot vibration generally focuses on the dynamic response characteristics of robots and the vibration situation of robots by establishing a dynamic model. However, this method involves complex robot modeling, computation, and parameter identification, and the accuracy of the results is limited. Herein, the static method analyzes the combined force acting on the robot's joints during welding [16]. Previous welding stability experiments showed that the force in the -y direction significantly impacts welding stability. Therefore, the force situation in the y-z plane will be mainly analyzed in the following part.

Figure 8 shows that the analysis of the torque was exerted on different joints of the FSW robot by the combined force acting on the robot end in the y-z plane during the welding process along the +y and -y directions. Among them, F_v is the combined force of the axial force F_d and the forward resistance force F_r in the y-z plane. O_2 , O_3 , and O_5 are the rotation centers of the robot's joints 2, 3, and 5, respectively. L_{a2} , L_{a3} , and L_{a5} represent the lengths of perpendicular lines drawn from O_2 , O_3 , and O_5 perpendicular to the F_v direction. Comparing Figure 8a with Figure 8b, when the feed direction was +y, the length of the force arm (L_{a2} , L_{a3}) that applied torque to O_2 and O_3 by the combined force F_v increased significantly compared to when the feed direction was -y. When the F_v value was the same, during the feed process along the +y direction, joints 2 and 3 bore greater torque than those along the -y direction. When the robot's end vibrated, the fluctuation of the end effector force during the feed process had a more significant impact on joints 2 and 3 along the +y direction than along the -y direction. As the direction of the welding force was fixed relative to the position of joint 5, the influence of welding direction on joint 5 was relatively small.

According to geometric relationships, it can be inferred that in any pose, the length of the robot's force arm of the combined welding force on the torque of joints 2 and 3 is shown in Equation (15):

$$L_{ai} = \frac{|({}^iP \times {}^iF)_z|}{\|{}^iF_{xy}\|}, (i = 2, 3) \quad (15)$$

where iP is the translation vector from joint i to the end of the robot, iF is the representation of welding force F_i in the joint i coordinate system ${}^iF = {}^iR \cdot F_i$, iR is the rotation matrix from joint i to the end of the robot, and ${}^iF_{xy}$ is iF in the x-y plane of the joint i coordinate system.

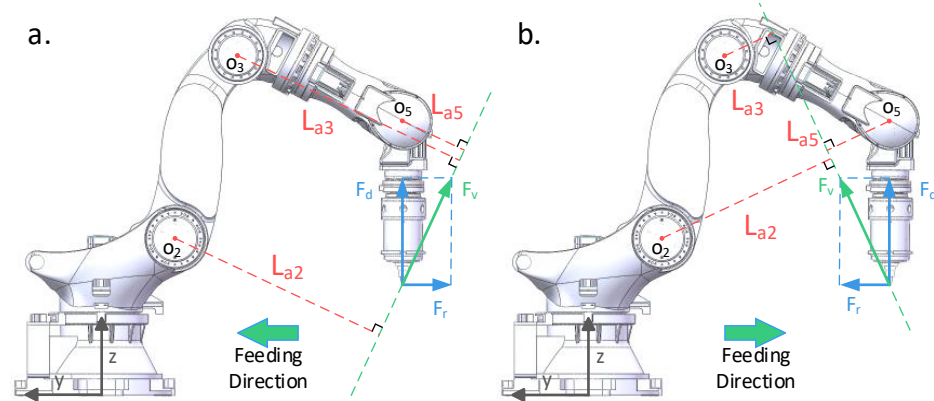


Figure 8. Analysis of joint torque in different welding directions. (a) The torque experienced by the robot joint when feeding in the +y direction. (b) The torque experienced by the robot joint when feeding in the −y direction.

Based on the above conclusions, it can be inferred that the length of the force arm of the combined welding force on the torque of joints 2 and 3 can be used as an evaluation index for the vibration stability of the robot under the current pose and force conditions. To comprehensively consider the weights of the two joint force arms, the average value was calculated, and the vibration stability index of the robot was obtained, as given by Equation (16).

$$L_a = \frac{L_{a2} + L_{a3}}{2} \quad (16)$$

Next, a new comprehensive stability index for FSW robots was established (Equation (17)) by combining the stiffness index of the robot's end direction with the vibration stability index. To prioritize ensuring the stability of robot vibration, the comprehensive stability index utilized the properties of inverse proportional functions. The directional stiffness index of the robot has a greater weight only when the vibration stability is optimal, as shown in Equation (17).

$$S = \frac{L_e}{1 + L_a} \quad (17)$$

The comprehensive stability index was used to score the four feed directions in the welding stability experiment. Experimental results showed that the axial force $F_d = 4842.58$ N, forward resistance force $F_r = 899.80$ N, and lateral force $F_l = 1350.87$ N. By inputting the welding force into the comprehensive stability index calculation formula corresponding to the feed direction, $S_{+x} = 0.1886$, $S_{-x} = 0.4832$, $S_{+y} = 0.1908$, and $S_{-y} = 0.3124$ were obtained. By comparing the calculated results with the experimental results, the welding process was the most stable along the −x direction, with the highest comprehensive stability coefficient. The welding stability was the worst along the +x direction, with the lowest comprehensive stability coefficient. The welding stability along the +y and −y directions was intermediate, and the welding stability along the −y direction was better than along the +y direction. The comprehensive stability coefficient can also reflect this. Therefore, the comprehensive stability coefficient can reflect the welding stability in different feed directions.

4. Optimization of Installation Position for Complex Space Curve Weldments

4.1. Comprehensive Stability Function of Complex Space Curve Weldments

The end performance of robots varied in different poses, and the performance in different feed directions also varied in the same pose. This added complexity to the pose and trajectory optimization of FSW robots. Especially when welding large and complex space curve welds, it is of great significance to study how to ensure the stability of robots during the welding process. When performing short-distance straight welding, the pose changes of the robot can often be ignored. Based on the robot pose at the starting point of

the weld, a stable welding direction can be calculated and selected. The characteristic of complex space curve welds is that the welding distance is long, and the welding direction is variable, resulting in significant changes in the robot's posture and end force.

The thin plate weldment shown in Figure 9a is a typical complex space curve weldment consisting of two thin aluminum alloy plates approximately 790 mm in length, 400 mm in width, and with a curved radius of 1550 mm. The workpiece was fixed using the fixture shown in Figure 9b. This fixture can be fixed on a flat, sturdy surface for performing FSW. The dimensions of the fixture are shown in Figure 9c. To achieve better welding quality, the robot was kept relatively stable when performing FSW tasks to optimize the stiffness and vibration stability. Furthermore, the robot end effector must have a fixed inclination angle with the weld and move uniformly along the weld trajectory. Once the position of the weld is determined, the end trajectory and pose of the robot cannot be changed. Therefore, optimizing the stability of robots is equivalent to optimizing the installation position of the weldments.

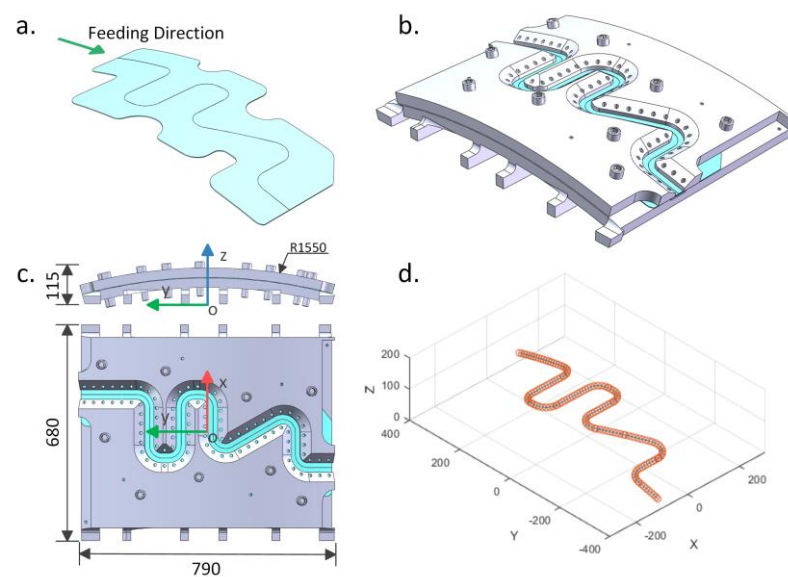


Figure 9. Complex space curve weldment. (a) Model of the weldment. (b) The weldment fixture. (c) Dimensions of the weldment fixture. (d) Trajectory of the weld seam.

The workpiece coordinate system was established (Figure 9c), and offline programming software (PQArt 2023) was used to extract the weld trajectory (Figure 9d). The weld trajectory was discretized into n trajectory points at fixed intervals $P = [P_1, P_2, \dots, P_n]$. The relative position vector between the workpiece coordinate system and the robot base coordinate system is $P_w = [x \ y \ z \ A \ B \ C]^T$, where x , y , and z are the workpiece coordinate system origin in the robot base coordinates (m). A , B , and C are the angles of rotation around the z , y , and x axes, respectively ($^\circ$). Based on the relative position vector P_w , the homogeneous transformation matrix of the workpiece coordinate system can be calculated relative to the robot base coordinate system ${}^0_w T$, as shown in Equation (18):

$${}^0_w T = R_z(A)R_y(B)R_x(C)T_p(x, y, z) \quad (18)$$

where R_z is the matrix rotating around the z -axis, R_y is the matrix rotating around the y -axis, R_x is the matrix rotating around the x -axis, and T_p is the translation matrix.

Thus, the end pose of the robot at the weld trajectory point can be found using Equation (19):

$$T_i = {}^0_w T P_i, (i = 1, 2, \dots, n) \quad (19)$$

According to T_i , the robot joint angle and Jacobian matrix at the current point can be obtained through the robot inverse solution operation. Assuming the welding force acting

on the end of the robot during the welding process is $F_t = [F_x \ F_y \ F_z]^T$ and is relatively stable, then based on Equation (17), the comprehensive stability coefficient of the robot at each point of the weld trajectory can be obtained, as shown in Equation (20).

$$S_i = \frac{L_e(T_i, F_t)}{1 + L_a(T_i, F_t)}, (i = 1, 2, \dots, n) \quad (20)$$

Thus, the comprehensive stability coefficient of the robot for the entire weld trajectory point can be obtained as in Equation (21).

$$S_p = \sum_{i=0}^n S_i = \sum_{i=0}^n \frac{L_e(T_i, F_t)}{1 + L_a(T_i, F_t)} \quad (21)$$

S_p represents the comprehensive stability evaluation index of the robot for the current welding position and welding parameters of the weldment. The larger the S_p , the higher the stability of the robot during the current welding task. Optimizing the welding process with S_p as the objective function can simplify the optimization process into finding the maximum value of the objective function.

4.2. Optimization of Weldments' Installation Position Using the PSO Algorithm

When optimizing the position of weldments using the robot's comprehensive stability function S_p as the objective function, it is necessary to consider the range of values of the independent variables, the robot's reachable space, and the limitations of the robot's joint angles. This is a typical constrained optimization problem. Using metaheuristic algorithms to solve constrained optimization problems is an effective and efficient choice [32]. The commonly used metaheuristic algorithms include the genetic algorithm (GA), particle swarm optimization (PSO), simulated annealing (SA), and so on. They all solve complex optimization problems by simulating specific phenomena or biological behaviors in nature. Among them, the GA has robust searchability and is suitable for multi-objective optimization problems, but its convergence speed is slow. The PSO algorithm has a fast convergence speed and performs well in a continuous space search but is prone to falling into local optima. The SA algorithm can be used for a discontinuous space search, with a probability of jumping out of local optima, and is suitable for solving large-scale complex problems. Still, it has a significant computational load and slow convergence speed [33]. To select the appropriate optimization algorithm, further analysis of the objective function S_p is required.

From Equation (21), the input parameter of S_p is the pose matrix of the robot at weld trajectory point T_i and welding force vector F_t . If the robot's end pose is kept relatively fixed with the welding direction while the weld trajectory remains unchanged, as shown in the coordinate system o_i in Figure 5a, then the welding force during the welding process can be regarded as a constant in the robot end coordinate system. At this point, the objective function S_p is only related to the relative position vector $P_w = [x \ y \ z \ A \ B \ C]^T$ of the weldment relative to the base coordinate. Equation (21) can be written as Equation (22):

$$S_p = f(P_w) = f(x_1, x_2, x_3, x_4, x_5, x_6) \quad (22)$$

The multivariate function shown in Equation (22) cannot visually determine the continuity of the function, like unary and binary functions. However, it is possible to infer the continuity of the function by fixing a portion of the independent variables and using dimensionality reduction visualization methods. Figure 10a shows the image of S_p when $P_w = [x \ y \ 0.8 \ 0 \ -20 \ -5]^T$, the value range of x is $[0, 3]$, the value range of y is $[-2, 2]$, and the value interval is 0.05. Figure 10b shows the image of S_p when $P_w = [1.8 \ 0.3 \ z \ A \ -20 \ -5]^T$, the value range of z is $[0, 2]$, the value range of A is $[-180, 180]$, and the value interval is 2. The image of S_p is shown in Figure 10c when

$P_w = [1.8 \ 0.3 \ 0.8 \ 0 \ B \ C]^T$, the value range of B is $[-90, 90]$, the value range of C is $[-90, 90]$, and the value interval is 2. The image in the figure has been adjusted in scale and display range.

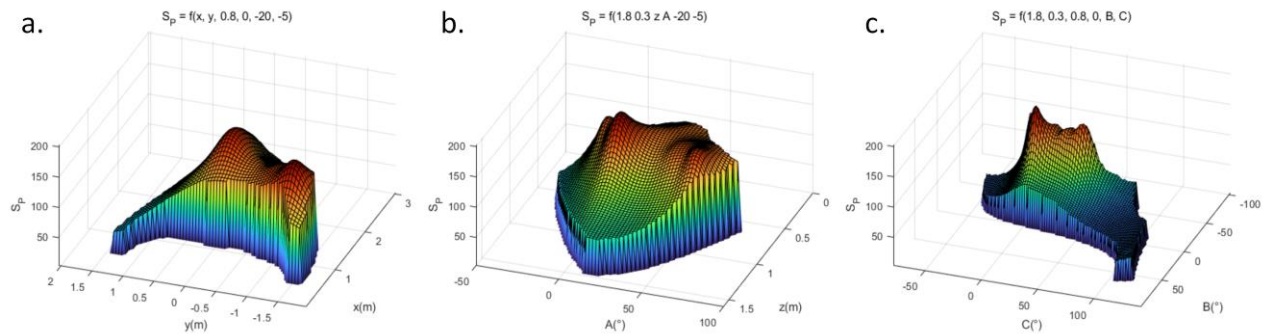


Figure 10. Function image obtained through dimensionality reduction visualization. (a) x, y as variables. (b) z, A as variables. (c) B, C as variables.

From the dimensionality reduction visualization of the objective function S_p (Figure 10), the distribution of data can be intuitively observed. The function value shows continuous variation within the effective range of the independent variable. The PSO algorithm has high applicability and fast convergence speed in a continuous space search, and it was chosen as the optimization algorithm for the objective function.

4.2.1. Standard PSO Algorithm

The PSO algorithm is an optimization technique based on swarm intelligence inspired by the collective behavior of the shoals of birds and fish. In this algorithm, each “particle” represents a potential solution that moves in the solution space, updating its position and velocity by tracking the historical best positions of individuals and populations. This method enables particle swarms to explore and find the optimal or near-optimal solution [34]. The optimization process of the PSO algorithm is as follows:

First, we initialized the particle swarm, set the population size N and the population dimension D according to the problem being solved, and obtained the initial position X_i and initial velocity V_i of the population. In PSO, the objective function is called the fitness function. After initializing the population, the current fitness of each particle was calculated using a fitness function; the optimal fitness P_{best} for each particle and the population optimal fitness G_{best} were obtained with their corresponding positions $X_{P_{best}}$ and $X_{G_{best}}$. Subsequently, we iterated and updated the speed and position of the current population according to the update rules, as shown in Equations (23) and (24) [34]:

$$V_{i+1} = w \cdot V_i + c_1 \cdot r_1 \cdot (X_{P_{best}} - X_i) + c_2 \cdot r_2 \cdot (X_{G_{best}} - X_i) \quad (23)$$

$$X_{i+1} = X_i + V_{i+1} \quad (24)$$

where V_{i+1} is the updated particle velocity, X_{i+1} is the updated particle position, V_i is the current particle velocity, X_i is the current particle position, $X_{P_{best}}$ is the optimal fitness position for the current particle, $X_{G_{best}}$ is the optimal fitness position for the current population, w is the inertia coefficient, c_1 is the self-learning factor, c_2 is the population learning factor, and r_1 and r_2 are random numbers between (0, 1).

The PSO algorithm can remember the historical best fitness positions of individual particles and the entire population and share the current global optimal information with the whole population. When the calculation started, the population was randomly distributed throughout the entire search space, and after iteration and updating, the population gathered near the extremum of the fitness function. When the number of iterations reached the maximum number of iterations G_k , we calculated termination and output the best fitness G_{best} of the current population and its corresponding position $X_{G_{best}}$.

Assuming that during the welding process, the force at the robot's end effector, consistent with the welding stability experiment, was $F_t = [-899.80 \ 1350.87 \ -4842.58]^T$, a constrained optimization problem model was established, as shown in Equation (25):

$$\begin{aligned} \text{Maximize} \quad & S_P = f(x_1, x_2, x_3, x_4, x_5, x_6) \\ \text{s.t.} \quad & \Theta_i = \text{IK}(P_i), (i = 1, 2, \dots, n) \\ & \Theta_{\min} < \Theta_i < \Theta_{\max} \\ & X_{\min} < X_i < X_{\max} \end{aligned} \quad (25)$$

where P_i represents the weld trajectory points; IK is the inverse kinematics solution of the robot at the current trajectory point; θ_i is the joint angle of the robot at the current trajectory point, where $\Theta = [\theta_1 \ \theta_2 \ \theta_3 \ \theta_4 \ \theta_5 \ \theta_6]$; X_i is the independent variable value at the current trajectory point, where $X = [x_1 \ x_2 \ x_3 \ x_4 \ x_5 \ x_6]$; Θ_{\min} and Θ_{\max} are the range of values for robot joint angles (their values are shown in Table 1); and X_{\min} and X_{\max} are the range of independent variables values, where $X_{\min} = [0 \ 0 \ 0 \ -180 \ -90 \ -90]$ and $X_{\max} = [3 \ 0 \ 2 \ 180 \ 90 \ 90]$.

Herein, by adjusting the independent variable x_2 , the value range was limited to (0,0), so that the origin position of the weld was limited to the x-z plane of the base coordinate system to reduce redundant solutions. For the population size $N = 50$, inertia coefficient $w = 0.5$, learning factor $c_1 = c_2 = 0.5$, number of iterations $G_k = 500$, and repeated calculation of 20 times, the results are shown in Figure 11. Figure 11a shows the convergence curve of the optimization process. From the graph, the entire process reached or approached the optimal value before 100 steps, and most processes reached or approached the optimal value before 50 steps.

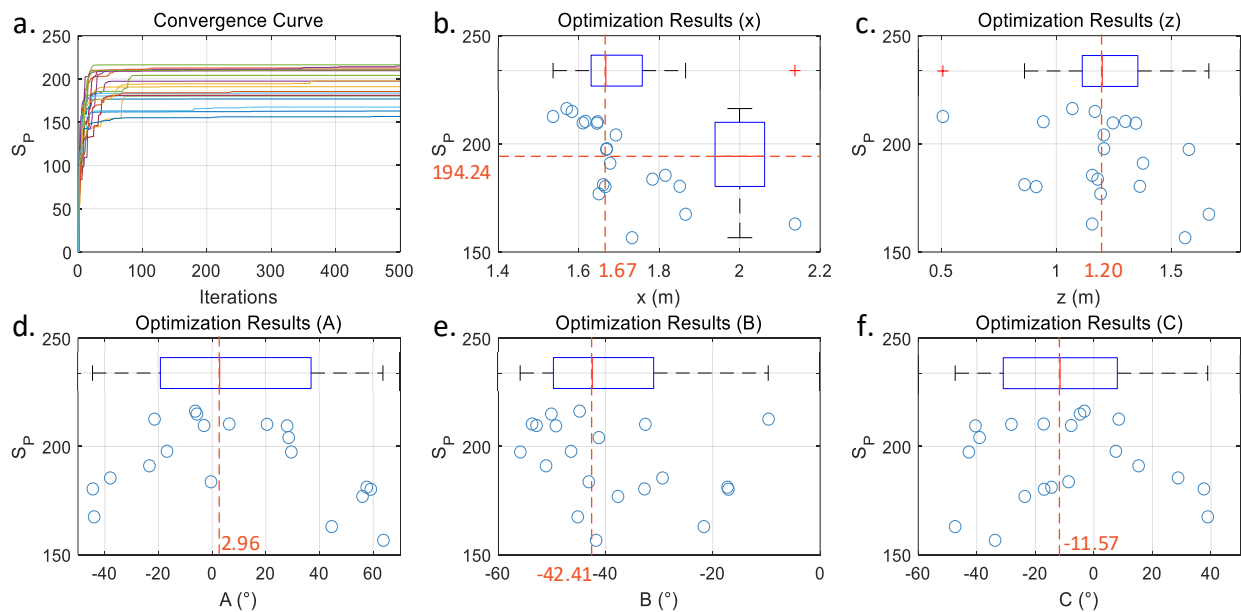


Figure 11. The standard PSO optimization results. (a) The convergence curve obtained from 20 optimization calculations. (b–f) The scatter plots and box plots of the optimization results.

It can be seen that the PSO algorithm can achieve a fast convergence speed under the current fitness function. After optimization, the final value of the fitness function S_P was between 150 and 220, and the results were relatively scattered, indicating the existence of multiple local extreme points in the current fitness function. The maximum fitness value calculated was $S_{P_{max}} = 216.31$, with an average $\mu_{S_P} = 194.44$ and a standard deviation $\sigma_{S_P} = 18.45$. The physical quantity corresponding to the independent variable of the fitness function was defined as the horizontal axis, and the fitness value was the vertical axis. The scatter plots and box plots of the optimized solution set are shown in Figure 11b–f. The

distribution of the solution set was relatively scattered within the defined domain and did not exhibit prominent clustering characteristics. The means and standard deviations of each independent variable solution set were calculated as follows: $\mu_x = 1.70$, $\sigma_x = 0.14$; $\mu_z = 1.20$, $\sigma_z = 0.27$; $\mu_A = 9.51$, $\sigma_A = 35.42$; $\mu_B = -38.66$, $\sigma_B = 13.59$; and $\mu_C = -9.58$, $\sigma_C = 26.12$.

From the results, the standard PSO algorithm performed poorly during the optimization process of the fitness function S_p . From the convergence curve, the particle swarm had a fast convergence speed and a slight change after 100 steps. Therefore, it is impossible to improve the optimization results by increasing the number of iteration steps. From the scatter plot, the local extremum points were often far apart in specific dimensions. Meanwhile, the multidimensional nature of the fitness function made it more difficult for the overall population to search for distant extreme points. Experiments found that modifying the inertia and learning factors can improve convergence speed and increase the probability of jumping out of local optima, but the effect is limited. Population size can improve the optimization results but will increase the computational burden. However, the search efficiency can be improved by reducing the number of iterations in a single optimization and increasing the number of calculations. According to the convergence curve, after 100 steps, most optimization processes still yielded better results, and reducing the number of iteration steps will lower the accuracy of exploitation.

4.2.2. Dynamic Dual PSO Algorithm

In response to the above situation, this study introduces a dynamic dual PSO (DDPSO) method. This method uses two sets of particle swarms referred to as P_1 and P_2 that do not affect each other but have a constant population size (N). Firstly, P_1 is in charge of exploitation, P_2 is responsible for exploration, $N_{P_1} = N$, and $N_{P_2} = 0$. Activating P_2 after P_1 results in an extreme point for a certain number of steps. The population size of P_2 is $N_{P_2} = N_{P_2} + \Delta N$, and the population size of P_1 is reduced by $N_{P_1} = N_{P_1} - \Delta N$. After both groups of particle swarms reach their extreme points and continue for a certain number of steps, if the fitness of P_2 is smaller than P_1 , then P_2 should be reinitialized, the initial population size ΔN should be increased, and the population size of P_1 should be reduced by ΔN . If the fitness of P_2 is consistently less than P_1 , the population size of P_2 should be further increased, and the population size of P_1 should be further reduced until the defined minimum value N_{min} . If the fitness of P_2 surpasses that of P_1 , the exploitation and exploration status of P_1 and P_2 should be transferred. The population size of P_2 should be adjusted as $N_{P_2} = N$, and then P_1 should be initialized and its population size adjusted as $N_{P_1} = 0$. Until P_2 falls to the extreme point for a certain number of steps, P_1 should be activated and the above steps repeated. After reaching the set maximum number of iterations, the maximum fitness of the population and its corresponding independent variables should be output as the optimization result. The flowchart is shown in Figure 12.

The DDPSO algorithm improves global search efficiency by dynamically adjusting the number of two populations without increasing computational burden while also considering the exploitation near existing extreme points, balancing the relationship between exploitation and exploration. Using the same population size as the standard PSO algorithm for optimization, $N = 50$, inertia coefficient $w = 0.5$, learning factor $c_1 = c_2 = 0.5$, number of iterations $G_k = 500$, and 20 optimization calculations were repeated. The optimization results obtained are shown in Figure 13. Figure 13a shows the convergence curve of a specific optimization process. The solid blue line represents the maximum fitness curve for P_1 ; the solid green line indicates the maximum fitness curve for P_2 ; and the red dashed line represents the overall maximum fitness curve, and its value is the larger value of the fitness of two populations.

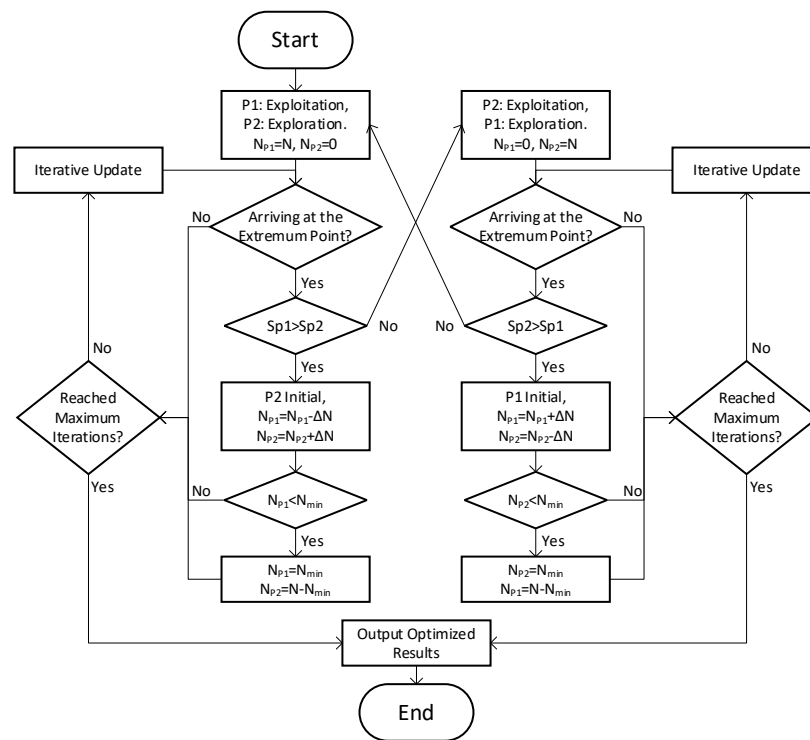


Figure 12. Flowchart of DDPSO algorithm.

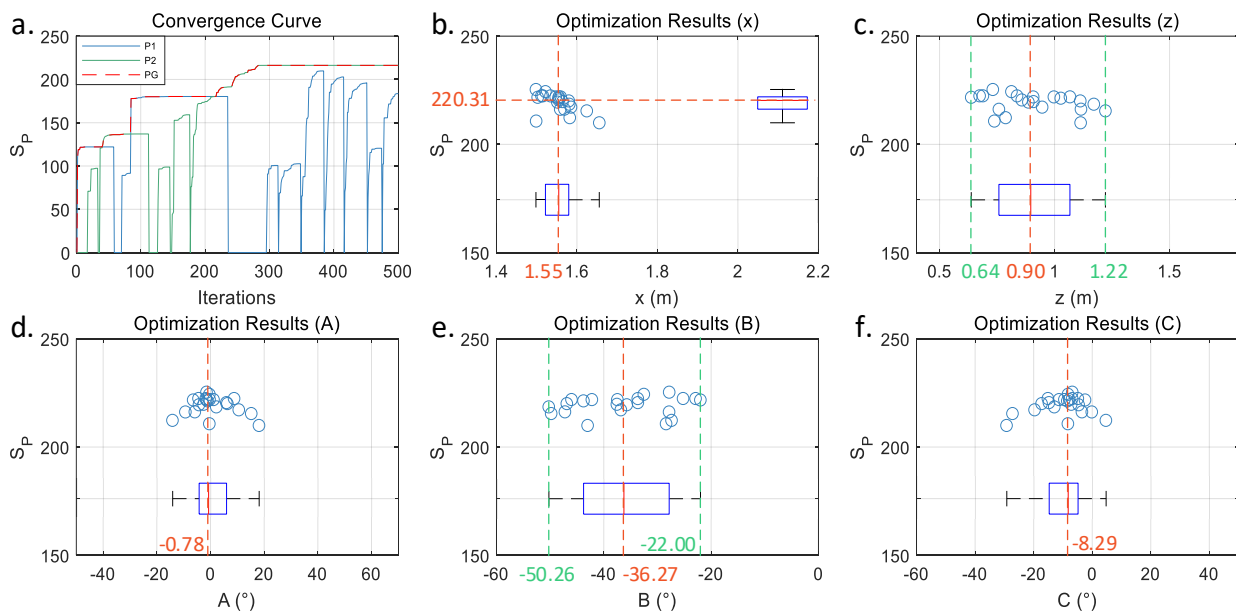


Figure 13. The DDPSO optimization results. (a) The convergence curve of an optimization calculation. (b–f) The scatter plots and box plots of the optimization results.

In the optimization calculation process, P_1 and P_2 underwent several transitions between exploration and exploitation. The optimization process effectively escaped from local optima through continuous exploitation and constant exploration. The maximum fitness value calculated was $Sp_{max} = 225.36$, with an average $\mu_{Sp} = 219.21$, and standard deviation $\sigma_{Sp} = 4.21$. Figure 13b–f shows the scatter plot and box plot of the relationship between the optimization results of the solution set and fitness. Figure 13 also shows that there was a significant clustering of solution sets in the results of x , A , and C , while in the results of z and B , the solution sets were evenly distributed within a specific region.

Therefore, it can be speculated that the optimal solutions for x , A , and C are located near the aggregation point of the solution set, while z and B have corresponding optimal solutions within a specific range. Further observation of the distribution of z and B revealed that their solution sets are approximately symmetrically distributed, indicating that z and B are two related variables. When calculating the optimal solution, one can be determined based on the actual situation to calculate the value of the other. The means and standard deviations of each independent variable solution were calculated as $\mu_x = 1.55$, $\sigma_x = 0.04$; $\mu_z = 0.91$, $\sigma_z = 0.17$; $\mu_A = 0.62$, $\sigma_A = 7.67$; $\mu_B = -36.28$, $\sigma_B = 8.90$; and $\mu_C = -10.10$, $\sigma_C = 8.11$.

The solution set of the optimization result was concentrated near a specific value, indicating a better solution for the current optimization process near this value. The higher the concentration, the higher the stability of the optimization method. The comparison and analysis between the optimization results of DDPSO and standard PSO are as follows. The maximum fitness value obtained by the DDPSO algorithm increased by 4.2% compared to the standard PSO, and the average value grew by 12.74%. Using the standard deviation as the concentration index, the fitness concentration of the DDPSO improved by 77.18%. The concentration of optimization results increased by 71.43% for x , 37.04% for z , 78.35% for A , 34.51% for B , and 68.95% for C . Due to the unique distribution characteristics of z and B , when they were not considered, the optimization results of DDPSO increased the average concentration level by 72.91% compared to standard PSO. Therefore, the DDPSO algorithm has a better and more stable search capability for the fitness function S_p , and the optimization results are closer to the optimal solution.

The red dashed line in the optimization result set shown in Figure 13b–f represents the median of the current solution set, which can be used as the final optimization result. The optimized position vector was arranged as $P_w^* = [1.55 \ 0 \ 0.90 \ -0.78 \ -36.27 \ -8.29]^T$ for the optimized weldment relative to the robot base coordinate system. The position of the weld trajectory in the robot base coordinates and the robot pose during the welding process were obtained by using P_w^* as the input, as shown in Figure 14a. Adding P_w^* by inputting the parameters into the 3D software (SOLIDWORKS 2020), the relative position model between the welding fixture and the robot was obtained (Figure 14b). According to this model, the position and angle of the heavy-duty positioner was adjusted (Figure 14c), providing a reference for offline programming and process optimization of RFSW.

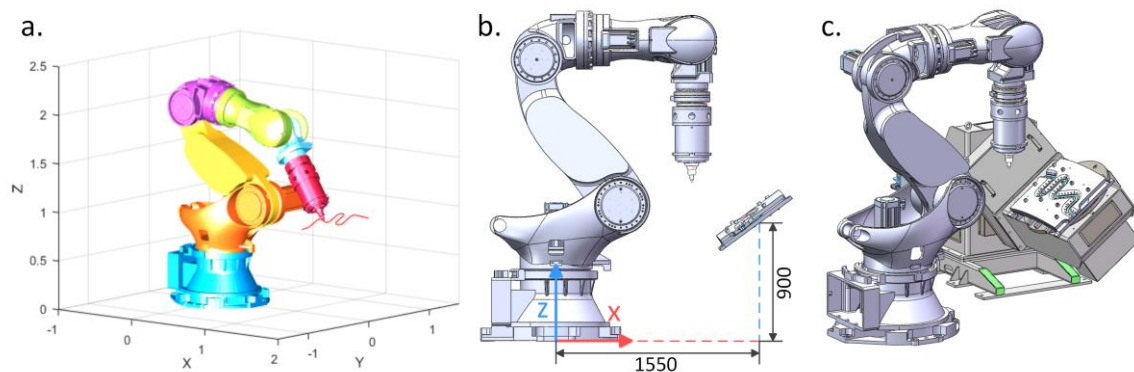


Figure 14. The optimized workpiece installation position. (a) The weld seam trajectory simulation result. (b) Weldment and robot's relative position. (c) Fixing the weldment using a positioner.

5. Conclusions

This study aimed to improve the stability of robots during the FSW process, focusing on the optimization of the installation position for complex space curve weldments. Initially, the directional stability of the robot during welding was analyzed through experiments. Subsequently, a dynamic dual particle swarm optimization algorithm was proposed, utilizing a comprehensive stability index for robots to optimize the installation position of complex space curve weldments. The conclusions are as follows:

- The stability of the FSW robot varies when welding in different directions. It is most stable in the $-x$ direction, followed by the $-y$ direction, with poorer stability in the $+y$ direction, and the worst in the $+x$ direction. The stabilities of each welding direction, represented by a comprehensive stability index, are $S_{+x} = 0.1886$, $S_{-x} = 0.4832$, $S_{+y} = 0.1908$, and $S_{-y} = 0.3124$. The higher the value, the better the stability, which is consistent with experimental results.
- When using the DDPSO method to optimize the position of weldments, it has better searchability and more stable optimization results than the standard PSO algorithm. The maximum fitness value obtained increased by 4.2%, the average value increased by 12.74%, and the concentration of optimization results increased by 72.91%.

There are still some limitations in this study. Although the optimized installation position of the weldment improved the overall stability of the weld trajectory, there were still a few parts of the trajectory that remained in poorer stability. Moreover, due to the inherent limitations of the FSW robot itself, significant deviations can still occur at the robot's end even in a pose with better stiffness. Additionally, the robot's natural frequency often falls within the common speed range of FSW, making it difficult to avoid resonance during welding. To address these issues, developing a robot positioner linkage control method, researching trajectory planning and error compensation methods under redundant degrees of freedom for RFSW, and studying methods for vibration avoidance/suppression for the robot could lead to better welding stability, thereby fully leveraging the advantages of RFSW.

Author Contributions: Conceptualization, S.C. and C.K.; methodology, S.C. and G.Z.; software, G.Z.; resources, S.C. and X.J.; writing—original draft preparation, G.Z.; writing—review and editing, X.J. and C.K. All authors have read and agreed to the published version of the manuscript.

Funding: This work was funded by the National Key Research and Development Program of China (2018YFB1306400), Shujun Chen, and “QiHang Programme” for the College of Mechanical and Energy Engineering, BJUT (QH202309), Xiaoqing Jiang.

Data Availability Statement: Data are contained within the article.

Conflicts of Interest: The authors declare no conflicts of interest.

References

1. Yue, W.; Liu, H.T.; Huang, T. An Approach for Predicting Stiffness of a 5-DOF Hybrid Robot for Friction Stir Welding. *Mech. Mach. Theory* **2022**, *175*, 23. [[CrossRef](#)]
2. Zhang, Y.M.; Yang, Y.-P.; Zhang, W.; Na, S.-J. Advanced welding manufacturing: A brief analysis and review of challenges and solutions. *J. Manuf. Sci. Eng.* **2020**, *142*, 110816. [[CrossRef](#)]
3. Yujie, B.; Haitao, L.; Shaofei, M.; Yue, M.; Wei, Y.; Guangxi, L.; Juliang, X.; Guofeng, W.; Yabin, D. An Approach for Predicting and Compensating the End Deformation of a Heavy Load Robot for Friction Stir Welding. *Mech. Mach. Sci.* **2023**, *147*, 673–682. [[CrossRef](#)]
4. Luo, H.T.; Wang, T.J.; Fu, J.; Chen, Z.C.; Leng, Y.Q. Analytical Kinematics and Working-condition Simulation for Friction Stir Welding (FSW) Robot. In Proceedings of the 2015 Ieee International Conference on Information and Automation, Lijiang, China, 8–10 August 2015; pp. 1992–1996.
5. Curiel, D.; Veiga, F.; Suarez, A.; Villanueva, P. Advances in Robotic Welding for Metallic Materials: Application of Inspection, Modeling, Monitoring and Automation Techniques. *Metals* **2023**, *13*, 711. [[CrossRef](#)]
6. Balaji, V.A.; Ajay, G.; Doss, A.S.A.; Schilberg, D. Analysis of Robotic Arm for Friction Stir Welding Application. *Lect. Notes Mech. Eng.* **2023**, 371–386. [[CrossRef](#)]
7. De Backer, J.; Christiansson, A.K.; Oqueka, J.; Bolmsjö, G. Investigation of path compensation methods for robotic friction stir welding. *Ind. Robot* **2012**, *39*, 601–608. [[CrossRef](#)]
8. Sun, L.F.; Fang, L.J. An approximation method for stiffness calculation of robotic arms with hybrid open- and closed-loop kinematic chains. *Adv. Mech. Eng.* **2018**, *10*, 12. [[CrossRef](#)]
9. De Backer, J.; Bolmsjö, G. Deflection model for robotic friction stir welding. *Ind. Robot.* **2014**, *41*, 365–372. [[CrossRef](#)]
10. Kolegain, K.; Leonard, F.; Zimmer-Chevret, S.; Ben Attar, A.; Abba, G. A feedforward deflection compensation scheme coupled with an offline path planning for robotic friction stir welding. *Ifac Pap.* **2018**, *51*, 728–733. [[CrossRef](#)]
11. Li, Z.W.; Zhao, H.H.; Zhang, X.C.; Dong, J.Y.; Hu, L.; Gao, H.M. Multi-parameter sensing of robotic friction stir welding based on laser circular scanning. *J. Manuf. Process.* **2023**, *89*, 92–104. [[CrossRef](#)]

12. Soron, M.; Kalaykov, I. A robot prototype for friction stir welding. In Proceedings of the 2006 IEEE Conference on Robotics, Automation and Mechatronics, Bangkok, Thailand, 1–3 June 2006; Volumes 1 and 2, p. 233.
13. Rahmi, M.; Abbasi, M. Friction stir vibration welding process: Modified version of friction stir welding process. *Int. J. Adv. Manuf. Technol.* **2017**, *90*, 141–151. [[CrossRef](#)]
14. Bagheri, B.; Abbasi, M.; Dadaei, M. Mechanical Behavior and Microstructure of AA6061-T6 Joints Made by Friction Stir Vibration Welding. *J. Mater. Eng. Perform.* **2020**, *29*, 1165–1175. [[CrossRef](#)]
15. Abbasi, M.; Bagheri, B.; Sharifi, F. Simulation and experimental study of dynamic recrystallization process during friction stir vibration welding of magnesium alloys. *Trans. Nonferrous Met. Soc. China* **2021**, *31*, 2626–2650. [[CrossRef](#)]
16. Zhanliang, Y. Research on Stiffness and Error Compensation Model of Friction Stir Welding Rbobot. Master's Thesis, Beijing University of Technology, Beijing, China, 2021.
17. Li, M.J.; Huang, D.X.; Han, H.B.; Yang, X.J. Chatter Detection and Identification in High-Efficient Robotic Milling CFRP Composites Using Acoustic Emission Technique. *Int. J. Precis. Eng. Anuf.-Gr Tech.* **2023**, *10*, 1155–1167. [[CrossRef](#)]
18. Ni, H.P.; Ji, S.; Ye, Y.X. Redundant Posture Optimization for 6R Robotic Milling Based on Piecewise-Global-Optimization-Strategy Considering Stiffness, Singularity and Joint-Limit. *Symmetry* **2022**, *14*, 2066. [[CrossRef](#)]
19. Nguyen, V.; Johnson, J.; Melkote, S. Active vibration suppression in robotic milling using optimal control. *Int. J. Mach. Tools Manuf.* **2020**, *152*, 11. [[CrossRef](#)]
20. Xin, S.; Peng, F.; Tang, X.; Wu, J.; Sun, Z.; Yan, R. A joint wearable structural reinforcing device for vibration suppression in robotic milling. *MM Sci. J.* **2023**, 6992–6998. [[CrossRef](#)]
21. Moradi, H.; Bakhtiari-Nejad, F.; Movahhedy, M.R.; Vossoughi, G. Stability improvement and regenerative chatter suppression in nonlinear milling process via tunable vibration absorber. *J. Sound Vib.* **2012**, *331*, 4668–4690. [[CrossRef](#)]
22. Guan, W.; Cui, L.; Liang, H.; Wang, D.P.; Huang, Y.M.; Li, M.; Li, X.G. The response of force characteristic to weld-forming process in friction stir welding assisted by machine learning. *Int. J. Mech. Sci.* **2023**, *253*, 15. [[CrossRef](#)]
23. Shah, L.H.; Walbridge, S.; Gerlich, A. Tool eccentricity in friction stir welding: A comprehensive review. *Sci. Technol. Weld. Join.* **2019**, *24*, 566–578. [[CrossRef](#)]
24. Mao, Y.Q.; Ke, L.M.; Liu, F.C.; Liu, Q.; Huang, C.P.; Xing, L. Effect of tool pin eccentricity on microstructure and mechanical properties in friction stir welded 7075 aluminum alloy thick plate. *Mater. Des.* **2014**, *62*, 334–343. [[CrossRef](#)]
25. Panzer, F.; Werz, M.; Weihe, S. Experimental investigation of the friction stir welding dynamics of 6000 series aluminum alloys. *Prod. Eng.* **2018**, *12*, 667–677. [[CrossRef](#)]
26. Grimm, A.; Schulze, S.; Silva, A.; Göbel, G.; Standfuss, J.; Brenner, B.; Beyer, E.; Füssel, U. Friction stir welding of light metals for industrial applications. *Mater. Today Proc.* **2015**, *2*, S169–S178. [[CrossRef](#)]
27. Jain, A.; Qin, J.; Abba, G. Optimal workplacement for robotic friction stir welding task. In Proceedings of the 3rd IFTOMM International Symposium on Robotics and Mechatronics, ISRM 2013, Singapore, 2–4 October 2013; pp. 696–705.
28. Zhao, J.; Duan, Y.X.; Xie, B.Y.; Zhang, Z.Q. FSW robot system dimensional optimization and trajectory planning based on soft stiffness indices. *J. Manuf. Process.* **2021**, *63*, 88–97. [[CrossRef](#)]
29. Xiao, J.; Wang, N.; Liu, H.; Yue, W.; Wang, J.; Zhao, H.; Gao, J. Optimization method of position of robot friction stir welding parts based on optimal stiffness interval. *Aeronaut. Manuf. Technol.* **2023**, *66*, 22–31. [[CrossRef](#)]
30. Chen, S.; Zong, G.; Kang, C.; Jiang, X. Digital Twin Virtual Welding Approach of Robotic Friction Stir Welding Based on Co-Simulation of FEA Model and Robotic Model. *Sensors* **2024**, *24*, 1001. [[CrossRef](#)] [[PubMed](#)]
31. Dumas, C.; Caro, S.; Garnier, S.; Furet, B. Joint stiffness identification of six-revolute industrial serial robots. *Robot. Comput.-Integr. Manuf.* **2011**, *27*, 881–888. [[CrossRef](#)]
32. Almufti, S.M. Vibrating Particles System Algorithm performance in solving Constrained Optimization Problem. *Acad. J. Nawroz Univ.* **2022**, *11*, 231–242. [[CrossRef](#)]
33. Joshi, M.; Gyanchandani, M.; Wadhvani, R. Analysis Of Genetic Algorithm, Particle Swarm Optimization and Simulated Annealing On Benchmark Functions. In Proceedings of the 2021 5th International Conference on Computing Methodologies and Communication (ICCMC), Erode, India, 8–10 April 2021; pp. 1152–1157.
34. Eberhart, R.; Kennedy, J. A new optimizer using particle swarm theory. In *MHS'95, Proceedings of the Sixth International Symposium on Micro Machine and Human Science, Nagoya, Japan, 4–6 October 1995*; IEEE: Piscataway, NJ, USA, 1995; pp. 39–43.

Disclaimer/Publisher's Note: The statements, opinions and data contained in all publications are solely those of the individual author(s) and contributor(s) and not of MDPI and/or the editor(s). MDPI and/or the editor(s) disclaim responsibility for any injury to people or property resulting from any ideas, methods, instructions or products referred to in the content.